nature communications

Article

https://doi.org/10.1038/s41467-025-58216-4

Molecular basis for human respiratory syncytial virus transcriptional regulator NS1 interactions with MED25

Received: 11 July 2024

Accepted: 13 March 2025

Published online: 25 March 2025

Check for updates

Parismita Kalita[1], Oam Khatavkar[2,6], Grace Uwase[2,6], Yulia Korshunova[2,6], Yuying Hu[1], Nicole D. Wagner[1,3], Jian Xu[1], Jiehong Pan[1], Jay C. Nix[4], Michael L. Gross[3], Steven L. Brody[1], Dominika Borek[5], Gaya K. Amarasinghe[2], Jacqueline E. Payton[2] & Daisy W. Leung[1,2]

The Mediator complex facilitates interactions between transcription factors and RNA polymerase II, a process that is required for host gene transcription, including in response to viral infections. Among the many subunits in the Mediator complex, the MED25 subunit has been shown to be a target for viral activators during infection. Here we provide the molecular basis for the interaction between human respiratory syncytial virus (hRSV) nonstructural 1 protein (NS1) and the activator interaction domain (ACID) of MED25. The X-ray crystal structure of the complex revealed that NS1 straddles and binds two faces of MED25 ACID. This interaction is distinct from previously known viral activators. Importantly, our data support the conformational flexibility of viral transcriptional regulators. Furthermore, ChIP-seq and RNA-seq analysis identified the ATF3 transcription factor and a role for NS1/Mediator/ATF3 interaction in host gene regulation in hRSV infections. Our findings provide a molecular basis for hRSV NS1-based regulation of host gene transcription and reveal how viruses exploit the conformational heterogeneity at fuzzy transcription activator interfaces.

Human respiratory syncytial virus (hRSV) infections are a significant global health and economic burden. In the United States, hRSV is the leading cause of hospitalization among infants[1,2]. Globally, hRSV accounts for over 3.6 million hRSV associated hospital admissions per year in children ≤ 5 years. Lower respiratory tract infections caused by hRSV predominantly affect young children, the elderly, and individuals with compromised immune systems[3–6]. hRSV infection typically presents with mild symptoms resembling a common cold but can lead to bronchiolitis and pneumonia in severe cases. Recently, three hRSV vaccines have been FDA approved for use for adults ≥ 60 years[7–9] and one for pregnant individuals[10]. However, a gap in protection remains for young children, suggesting that we can improve our understanding of the host-viral interactions that occur during hRSV infection, which can allow for the development of additional countermeasures for hRSV and improved efficacy of already approved vaccines and therapeutics.

hRSV is a pneumovirus that targets the host transcriptional machinery upon infection to modulate gene expression, including host immune response genes[11–13]. hRSV encodes for the nonstructural protein 1 (NS1), which functions as a potent interferon (IFN) antagonist that leads to suppression of IFN signaling and immune responses[14,15]. We previously showed that NS1 is a structural paralog of the hRSV matrix (M) protein and adopts a similar structural fold as the

[1]Department of Medicine, Washington University School of Medicine, St. Louis, MO, USA. [2]Department of Pathology and Immunology, Washington University School of Medicine, St. Louis, MO, USA. [3]Department of Chemistry, Washington University in St. Louis, St. Louis, MO, USA. [4]Molecular Biology Consortium, Advanced Light Source, Lawrence Berkeley National Laboratory, Berkeley, California, USA. [5]Departments of Biophysics and Biochemistry, University of Texas Southwestern Medical Center, Dallas, TX, USA. [6]These authors contributed equally: Oam Khatavkar, Grace Uwase, Yulia Korshunova.
e-mail: dwleung@wustl.edu

N-terminal domain of M, containing a seven-stranded β-barrel flanked by three alpha helices[16]. We also identified a structured helical region unique to NS1 at the C-terminus (α3 helix) that is critical for NS1-mediated immunomodulatory functions. Mutations in the NS1 α3 helix resulted in attenuated immune response expression profiles in cells infected with recombinant hRSV[16]. Furthermore, we and others demonstrated that NS1 partitions into the nucleus upon hRSV infection in the A549 cell line and primary human tracheobronchial epithelial cells (hTBECs) and identified associations of NS1 with the Mediator complex, a coactivator of RNA polymerase II (Pol II) that bridges interactions between enhancers and promoters to initiate gene transcription[17–20]. Chromatin mapping of NS1 binding revealed colocalization with Mediator complex near regulatory elements of genes differentially expressed during hRSV infection, including STAT1 and IRF1[17]. How NS1 modulates transcriptional activation and innate immune responses to hRSV infection through the Mediator complex remain unclear.

The human Mediator complex is comprised of ~30 subunits. Nominally, these subunits are organized into 4 modules termed the head, middle, tail, and CDK8-associated regions. Many of these subunits within different modules bind to multiple transcription factors and relay signals that control Pol II-mediated transcription initiation, elongation, and termination[21–23]. These factors bind at enhancer and promoter regions, which may be quite distant from each other, via chromatin looping. Thus, the Mediator complex bridges the physical gap between transcription factors that control and produce RNA transcripts to modulate and refine the level and timing of gene transcription. Prior studies found that DNA viruses and retroviruses hijack the Mediator complex to activate and maintain high levels of viral gene transcription. For example, herpes simplex virus (HSV) protein VP16 is known to target the Mediator complex. The transcriptional activation domain (TAD) of HSV VP16 binds directly to the C-terminal activator interaction domain (ACID) of the MED25 subunit[24,25]. Mutation of residues in a hydrophobic groove of MED25 ACID disrupted VP16 binding and prevented transcriptional activation in vitro. Varicella zoster virus IE62 protein also contains a TAD that binds to the same region of MED25 ACID as VP16[26,27]. Other viruses, including small DNA tumor viruses, lymphotropic retroviruses, herpesviruses, dengue and Bunyamwera viruses, target different subunits in Mediator to control host gene expression and effectively block apoptosis, promote cell proliferation, and regulate metabolism[28]. However, the molecular interactions between RNA viral proteins and the Mediator complex or the transcriptional machinery, including transcription factors, are not well characterized to date.

To address this gap and to define the molecular basis for and the consequences of hRSV NS1 nuclear translocation, here we characterize the molecular interaction between hRSV NS1 and the MED25 subunit of Mediator complex and describe its functional impact on host gene transcription. NS1 binds with high affinity to the ACID domain of MED25 in equimolar ratio. Analysis of the NS1/MED25 ACID X-ray crystal structure revealed that NS1 and MED25 ACID share similar folds, each consisting of a core seven-stranded β-barrel that is surrounded by α-helices. NS1 interacts across two surfaces of MED25 ACID; the NS1 α3 helix binds to a hydrophobic groove formed by the β-barrel and terminal α-helices on one face of the MED25 ACID whereas Glu110 and Lys112 on the seventh β-strand of NS1 forms electrostatic interactions on the opposite face of MED25 ACID. Mutations of residues in the NS1 α3 helix or Glu110 disrupt binding to MED25 ACID. In addition, analysis of NS1 and Mediator chromatin immunoprecipitation sequencing (ChIP-seq) with bulk RNAseq from A549 cells and hTBECs transfected or infected with WT or Y125A NS1 hRSV defined differentially expressed genes (DEG) with NS1/Mediator binding. Because Mediator transduces signals from transcription factors (TF) bound at enhancers, we also evaluated transcription factor (TF) ChIPseq from a large public database for unbiased identification of TFs enriched at NS1/Mediator-bound DEGs. Activating transcription factor 3 (ATF3) was the most differentially expressed TF with the greatest number of DEG targets also bound by NS1 and Mediator complex. CUT&RUN sequencing of A549 cells expressing NS1 confirmed chromatin co-binding of NS1, Mediator, and ATF3 peaks at DEGs, with enrichment for immune response pathways. Further in vitro validation revealed that MED25 ACID directly binds to dsDNA bound-ATF3 and that the NS1 binding to MED25 ACID modestly reduces the binding affinity to ATF3. Moreover, mutations in NS1 that disrupt binding to MED25 ACID also reduced NS1 binding to chromatin and reduced the negative impact of NS1 on transcriptional activity. Altogether, our results identify hRSV NS1 as a viral interactor of MED25 that modulates Mediator complex and ATF3-associated transcriptional activity in response to hRSV infections through structural mimicry at fuzzy interfaces with a high level of conformational heterogeneity.

Results

NS1 directly binds the MED25 subunit

We and others previously found that hRSV NS1 associates with Mediator complex, including MED1, MED14, and MED25 subunits[17,19,20,29]. Of these subunits, proteins from multiple viruses hijack MED25 to enhance expression of viral genes[28]. MED25 contains two domains: an N-terminal von Willebrand factor type A domain (VWA), which links MED25 to the tail module of Mediator complex containing MED16, MED23, and MED24[21,30,31] and is connected by a disordered linker to a C-terminal activator interaction domain (ACID) (Fig. 1A). Prior studies revealed that proteins from the dsDNA viruses herpes simplex virus (HSV) and varicella zoster virus, VP16 and IE62 respectively, each bind to two different interfaces of MED25 ACID, named the "H1" and "H2" binding sites for the VP16 TAD subdomains[24–27]. To test if NS1 similarly binds to MED25, we first performed in vitro pulldown assays using recombinantly expressed and purified proteins. MBP-tagged NS1 (MBP-NS1) was immobilized onto amylose resin prior to incubation with MED25 ACID. We found that MBP-NS1 can pull down MED25 ACID, indicating a direct interaction whereas the control MBP protein alone does not bind MED25 ACID (Fig. 1B). To test if NS1 binds to MED25 VWA, GST-tagged MED25 VWA (GST-MED25 VWA) was immobilized onto glutathione sepharose resin and incubated with untagged NS1. Results from the pulldown assay did not show any binding of NS1 to MED25 VWA (Fig. 1B).

To further characterize the binding between NS1 and MED25 ACID in solution, we next performed size-exclusion chromatography coupled to multiangle light scattering (SEC-MALS) using a copurified complex of NS1/MED25 ACID (Fig. 1C, inset). NS1/MED25 ACID elutes in the included volume as a heterodimeric complex with a determined molecular weight of 33.7 ± 0.18 kDa and 0.99 polydispersity (M_w/M_n), whereas NS1 and MED25 ACID have individually determined molecular weights of 18.8 ± 1.4 kDa and 20.4 ± 1.4 kDa, respectively (Fig. 1C). We further assessed the interaction quantitatively using isothermal titration calorimetry (ITC). These results show that NS1 binds to MED25 ACID with high affinity (K_D = 41 ± 5 nM) (Figs. 1C, Table S2). Additional analysis of the SEC-MALS and ITC data reveal that NS1 binds MED25 ACID with 1:1 stoichiometry. Our observations here are similar to those previously reported[19,29].

Structure of the NS1/MED25 ACID complex

The structure of NS1 alone indicated that NS1 is likely a dynamic molecule, made evident by the increased flexibility of the region connecting the β-barrel to the α3 helix and the increased solvent accessible surface area of the α3 helix[16]. HDX-MS experiments also support the conformational flexibility of NS1, where peptides in the linker and α3 helix show high deuterium uptake extents, especially at later timepoints (many greater than 60%) (Fig. S1) and suggests that the dynamics of the α3 helix may depend on the local environment. This raises the possibility that NS1 may adopt a different conformation

https://doi.org/10.1038/s41467-025-58216-4

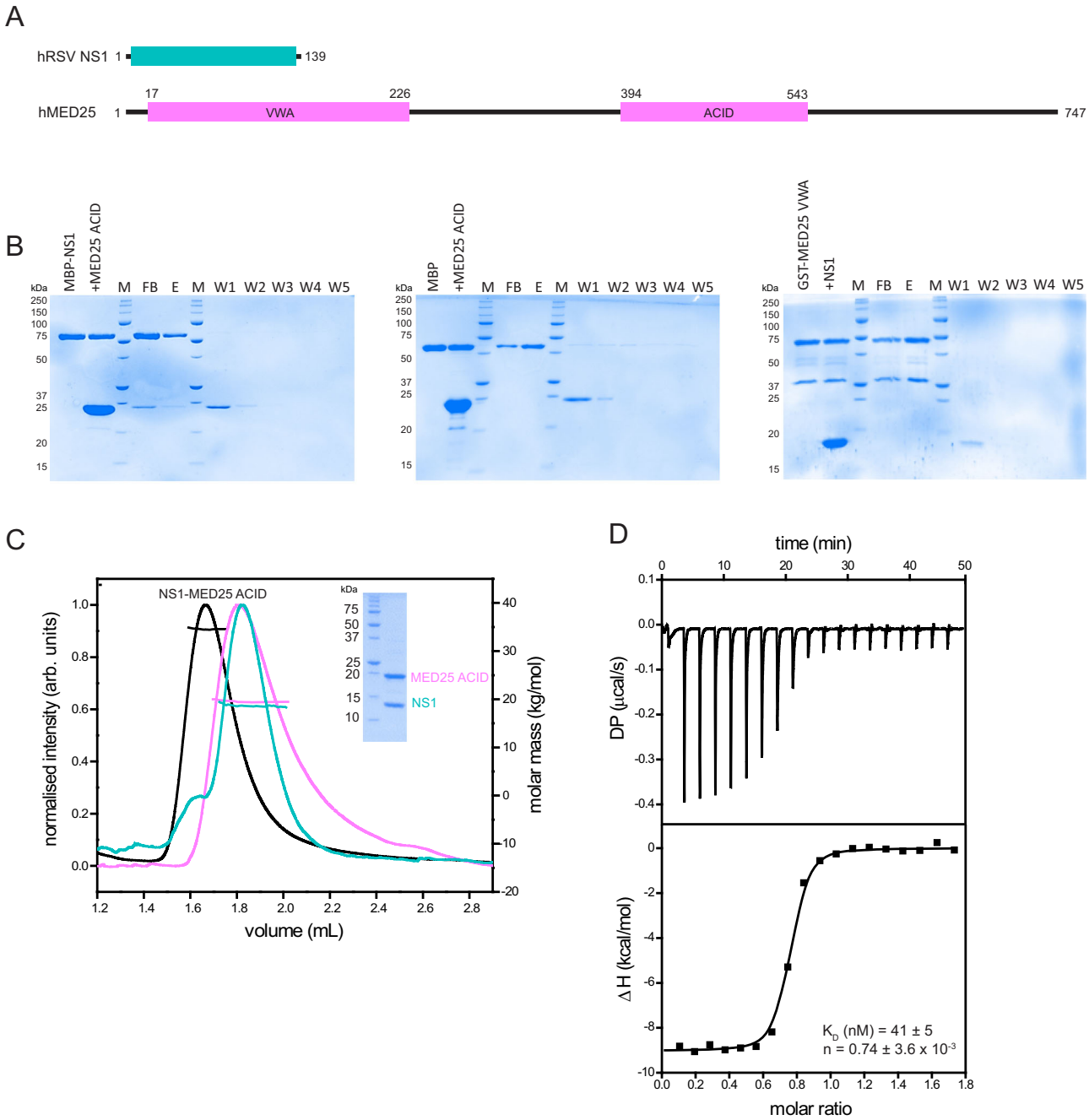

Fig. 1 | hRSV NS1 binds hMED25 ACID with high affinity. A Domain organization of NS1 and MED25. MED25 contains an N-terminal von Willebrand factor A domain (VWA) and a C-terminal activator interactor domain (ACID). In vitro pulldown assays for **B** MBP-NS1 with MED25 ACID (left), MBP with MED25 ACID (middle), and GST-MED25 VWA with NS1 (right). M, marker; FB, final beads; E, eluate; W, wash. Data shown is a representative of three independent experiments. **C** SEC-MALS analysis of the NS1/MED25 ACID complex (black) with a determined molecular weight of 33.7 ± 0.18 kDa compared to NS1 alone (teal) and MED25 ACID alone (violet). Inset, Coomassie stained SDS-PAGE of the protein complex. Data shown is a representative of three independent experiments. **D** Raw data and binding isotherm for MED25 ACID binding to NS1 measured by ITC. Data shown is a representative of three independent experiments.

when bound to a binding partner. We next solved the X-ray crystal structure of the NS1/MED25 ACID complex at 2.5 Å resolution. The asymmetric unit contains one molecule each of NS1 and MED25 ACID (Figs. 2A, Fig. S2A–B). The NS1 structure is a seven-stranded β-barrel where all β-strands (β1-β6) run antiparallel except β7 that runs parallel to β4, like the previously determined structure of NS1 alone (PDB ID 5VJ2)[16,32] and similar to the N-terminal domain of hRSV matrix (M) protein (PDB ID 2VQP)[16,32]. The β-barrel is flanked by three α-helices where the α1 and α2 helices are located on one end of the β-barrel and the α3 helix is connected by a flexible linker from β7 and is extended away from the β-barrel. The terminal five residues, including ^{136}DLNP^{139} that is in common with hRSV NS2[17], are disordered.

The MED25 ACID structure also contains a seven-stranded β-barrel that is surrounded by four α-helices (Figs. 2A, Fig. S2B), as was reported previously[24,25,33,34]. All MED25 ACID β-strands are antiparallel except β3 that runs parallel to β1 corresponding to β7 and β4 in NS1 (Fig. S2B). MED25 ACID β1 is connected to β2 by a flexible linker with poor electron density for the region between residues Pro412 to Lys422 that was therefore unmodeled. The α3 helix flanks one end of the β-barrel and the two 3_{10} helices, α1 and α2, are located on one side

https://doi.org/10.1038/s41467-025-58216-4

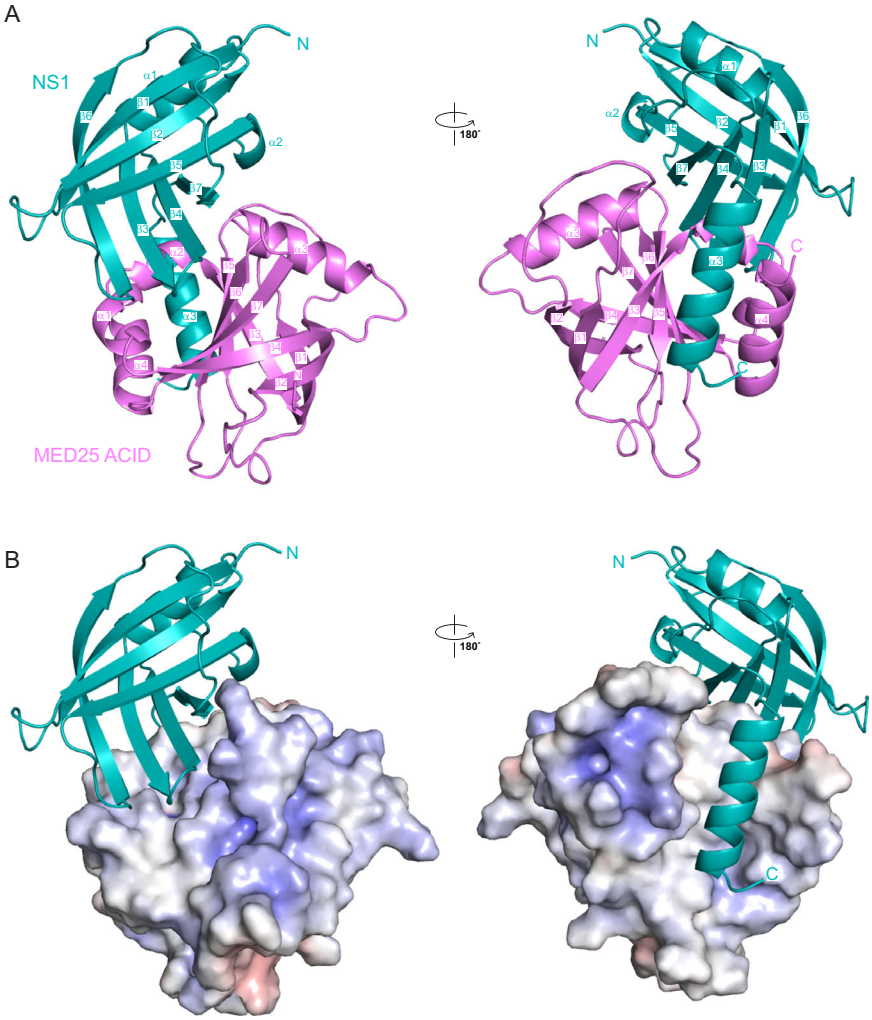

Fig. 2 | Structure of the NS1/MED25 ACID complex. A The 1:1 complex of NS1/MED25 ACID in ribbon representation with MED25 ACID oriented to show the "H2" binding site (left) and in a 180° rotated configuration to show the "H1" binding site (right). NS1, teal; MED25 ACID; violet. **B** Analysis of the NS1/MED25 ACID complex reveals extensive hydrophobic interactions and surface complementarity among residues at the interface. Electrostatic surface representation of MED25 ACID with NS1 in ribbon representation. Red, white, and blue represent negative, neutral, and positive electrostatic potential, respectively (−10 to +10 k_BT e-1). Orientations are as in **A**.

of the β-barrel along with α4 and close to the β6 and β7 strands. The β3, β5, and β6 strands, and the α4 helix are arranged such that a hydrophobic groove is formed that is lined with residues Ile537, Ile541, and Gln451 (Fig. 2B). The resemblance in arrangement of secondary structural elements prompted a structural comparison between NS1 and MED25 ACID. Structural superposition of the NS1 structure with MED25 ACID using GESAMT[35] yielded a root-mean-square deviation (RMSD) of 3.68 Å over 77 residues (Fig. S2C). While the NS1 and MED25 ACID β-barrel structures can be aligned, there are significant differences in the arrangement of loops and α-helices.

Analysis of the overall structure of the NS1/MED25 ACID complex revealed that NS1 and MED25 ACID are adjacent to each other with the NS1 β-barrel located on one side of the MED25 ACID β-barrel closest to the β6 and β7 strands and flanked by the MED25 ACID α1 helix ("H2" binding site[24,25]) (Fig. 2). NS1 binding to MED25 ACID is mediated by two interfaces: an electrostatic interface and a hydrophobic interface. Electrostatic interactions form between His58 in the NS1 β4 strand with MED25 ACID Gln456 in the first 3_{10} helix and Asn85 at the base of the NS1 β6 strand with MED25 ACID Arg466 in the α3 helix (Figs. 3A, Fig. S2D). Interestingly, MED25 ACID Arg466 is conserved amongst ACID homologs and was shown to be critical for binding to VP16[24,25]. Additional electrostatic interactions and hydrogen bonding are formed between Glu110 and Lys112 at the base of the NS1 β7 strand with MED25 ACID residues Ser516, Ser517, and Lys518 located in the linker between the β6 and β7 strands (Fig. 3A, B). Hydrophobic interactions are largely driven through contacts between the NS1 α3 helix that straddles the MED25 ACID β-barrel and sits in the hydrophobic groove lined by MED25 ACID residues including Gln451, Ile537, Ile541 ("H1" binding site[24,25]). NS1 α3 helix residues Tyr125, Leu132, and Leu133 residues are buried within this pocket (Figs. 2, 3A, 3C).

Analysis of shape complementarity (Sc) in the complex determined a value of 0.68 for the NS1 α3 helix and MED25 ACID, where a value of 1.0 indicates perfect complementarity[36]. Of the 6753.3 Å^2 and 6386.2 Å^2 of available surface area for NS1 and MED25 ACID, respectively, ~3867.3 Å^2 are in contact between NS1 and MED25 ACID. Furthermore, ~2856.6 Å^2 of surface area are in contact through interactions between the NS1 α3 helix and MED25 ACID, suggesting that interactions between NS1 α3 helix and MED25 significantly contribute toward complex formation. Together, these data support the protein-protein interactions observed in the structure.

NS1 straddles two sides of MED25 ACID

We previously demonstrated the importance of the NS1 α3 helix and specific residues within this helix in mediating IFN antagonism and modulating host transcription[16,17]. To further define a role for the NS1 α3 helix in the NS1/MED25 ACID interaction, we tested NS1 mutants

https://doi.org/10.1038/s41467-025-58216-4

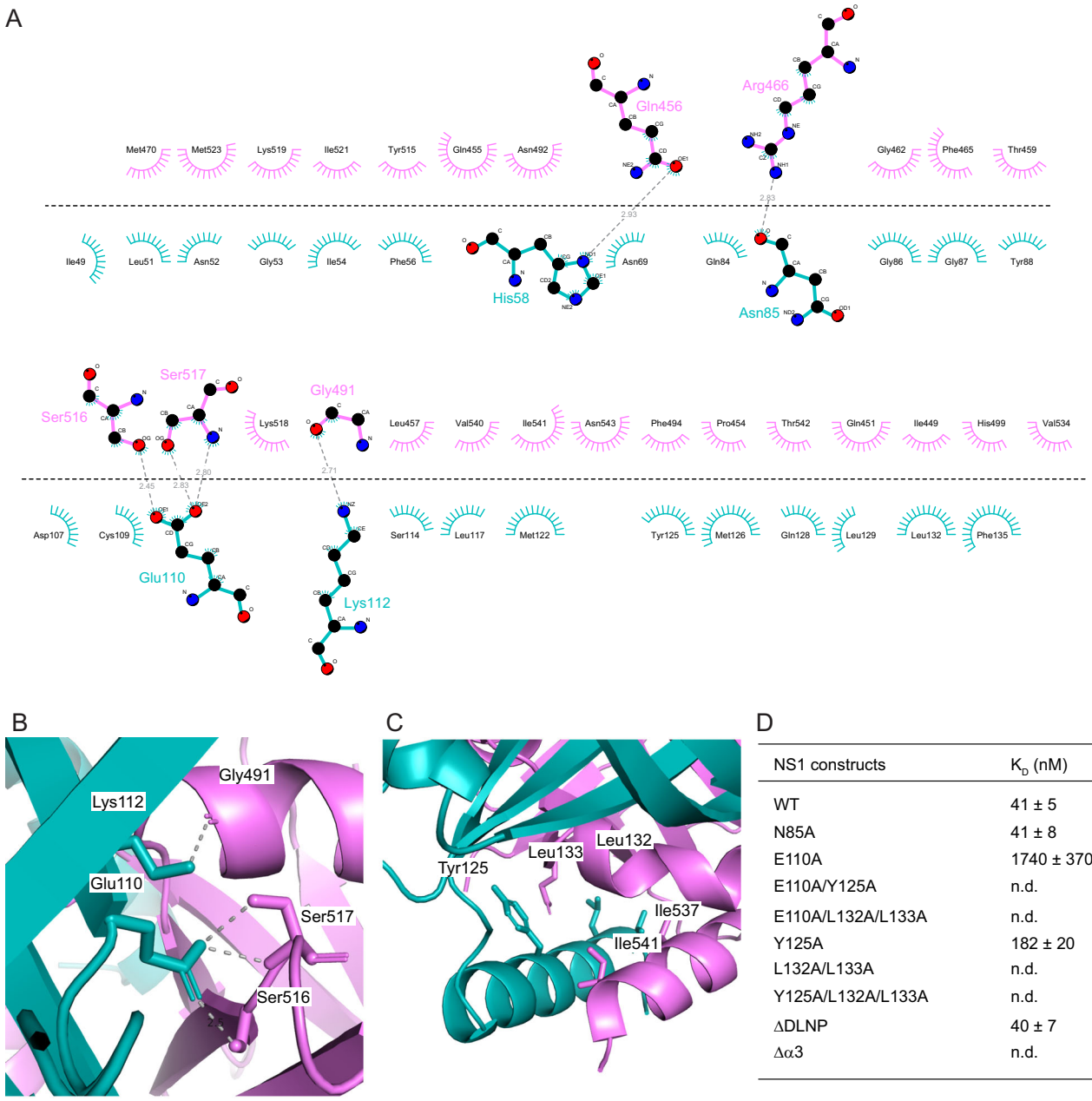

NS1 constructs	K_D (nM)
WT	41 ± 5
N85A	41 ± 8
E110A	1740 ± 370
E110A/Y125A	n.d.
E110A/L132A/L133A	n.d.
Y125A	182 ± 20
L132A/L133A	n.d.
Y125A/L132A/L133A	n.d.
ΔDLNP	40 ± 7
Δα3	n.d.

Fig. 3 | Analysis of the NS1 binding site on MED25 ACID. A LigPlot+ diagram shows extensive hydrophobic and hydrogen bond interactions between NS1 and MED25 ACID. **B**–**D** Ribbon representation highlighting the interaction between NS1 (teal) and MED25 ACID (violet). **B** NS1 E110 and MED25 S516, S517, and K518 residues are shown in stick representation. **C** NS1 Y125, L132, and L133 and MED25 I537 and I541 residues are shown in stick representation. **D** Summary of ITC binding measurements between NS1 mutants and MED25 ACID reveal residues that are necessary for high affinity binding. n.d., not determined.

Δα3, Y125A, and L132A/L133A for binding to MED25 ACID by in vitro pulldown assays and ITC experiments (Figs. 3D, Fig. S3). Deletion of the NS1 α3 helix (NS1 Δα3) resulted in the complete loss of binding to MED25 ACID, confirming the importance of the α3 helix in NS1 function. To ensure that mutation of NS1 did not impact the overall stability of the protein, we evaluated NS1 Δα3 and other mutants described below using a thermal shift assay. We observed no significant differences in NS1 protein stability for different NS1 mutations (Fig. S4A). NS1 mutant Y125A displayed a 4.5-fold decrease in binding to MED25 ACID ($K_D = 182 \pm 20$ nM,) compared to NS1 wildtype (WT) ($K_D = 41 \pm 5$ nM). We could not detect any MED25 ACID binding to NS1 mutant L132A/L133A or to the combined NS1 mutant Y125A/L132A/L133A like NS1 Δα3. We also tested mutation of corresponding residues in MED25 ACID, including I537A/R538A and I541A/T542A located on the α4 helix that contributes to the hydrophobic groove. While MED25 ACID I537A/R538A showed reduced stability compared to MED25 ACID WT and I541A/T542A (Fig. S4B), there was moderate impact on binding to NS1 (I537A/R538A, $K_D = 82 \pm 10$ nM; I541A/T542A, 116 ± 30 nM, respectively) (Fig. S5). Truncation of the four terminal residues ^{136}DLNP^{139} in NS1 (NS1 ΔDLNP) had no detectable impact on NS1/MED25 ACID interaction (Fig. 3D, Fig. S3).

We generated additional mutations based upon the NS1/MED25 ACID complex structure to evaluate the contribution of charged residues and hydrogen bonding in driving intermolecular interactions. Mutation of NS1 Asn85 to alanine had no impact on binding to MED25 ACID as the binding affinity ($K_D = 41 \pm 8$ nM) is similar to that of NS1 WT (Figs. S3, Table S2). Mutation of the corresponding residue Arg466 in MED25 ACID also had no impact on NS1 binding ($K_D = 47 \pm 10$ nM), despite the role this residue has in binding HSV VP16[24,25]. However, mutation of NS1 Glu110 to alanine led to significant loss of binding to

MED25 ACID both in in vitro pulldown assays and by ITC (K_D = 1740 ± 370 nM) (Figs. 3, Fig. S3), suggesting that Glu110 is a critical residue that facilitates NS1 binding to MED25 ACID. Combining the mutation of Glu110 with that of Y125 or L132/L133 in the NS1 α3 helix is sufficient to eliminate binding to MED25 ACID altogether. Furthermore, mutation of the corresponding residues Ser517 and Lys518 on MED25 ACID that form salt bridges with NS1 Glu110 (Figs. 4, Fig. S5) does not lead to a complete loss of binding to NS1 but an 8-fold reduction in binding affinity (K_D = 307 ± 80 nM). Altogether, these data suggest that multiple contacts are important for driving binding between NS1 and MED25 ACID.

NS1 localizes to genes targeted by the ATF3 transcription factor

To understand the functional significance of NS1 binding to MED25, we hypothesized that NS1 binding to MED25 modulates Mediator interaction with host transcription factors (TFs) that are important for host response to hRSV infection. To identify likely interacting TFs, we performed an integrative analysis of ChIP-seq (NS1 and Mediator) and RNAseq datasets that we collected from A549 cells and hTBECs transfected or infected with WT or Y125A NS1 hRSV. The goal of this initial analysis was to identify TFs with chromatin binding that overlaps with Mediator and NS1 at genes differentially expressed during hRSV infection (Fig. 4A). Genome annotation analysis revealed that NS1 peaks were located predominantly in genic regions, including promoter, exonic, and intronic regions (total 59%), compared to distal regions that primarily overlap with enhancer gene regulatory regions. Compared to NS1 peaks, NS1-Mediator peaks were more enriched in proximal promoter regions (≤ 1 kb, 18.7 vs 13.8%), with fewer peaks in introns and distal intergenic regions (Fig. 4B).

We previously reported that NS1-Mediator peaks are located at promoters and enhancers of immune response genes that are differentially expressed during RSV infection[17]. To identify TFs that may regulate the expression of genes with NS1-Mediator peaks for experimental study, we leveraged the ReMap2022 database, which contains > 8000 datasets representing whole genome binding data (ChIPseq) from > 1200 transcriptional regulators from > 700 human cells and tissues, including A549 cells[37]. This intersection yielded 529 TFs that bind at genes with NS1-Mediator peaks, reflecting the large number of cell lines and TFs in the ReMap2022 database (Fig. 4C, Supplementary Data 1).

To prioritize those that are most likely to be relevant for the NS1-Mediator interaction, we next evaluated expression of the genes with NS1-Mediator peaks using multiple RNAseq studies. We had previously determined that the Y125A mutation disrupts binding of NS1 to chromatin and transcriptional modulation of host immune response, notably for multiple interferon and chemokine signaling factors[16,17]. Therefore, we identified DEGs in A549 cells expressing NS1 WT versus NS1 Y125A and in cells infected with hRSV WT versus hRSV NS1 Y125A. To focus on DEGs in primary respiratory epithelial cells infected with RSV, we performed RNAseq on human tracheobronchial epithelial cells (hTBECs) differentiated in an air liquid interface (ALI) culture and then infected with hRSV at MOI 3 for 72 h. Overall, the patterns of expression are similar to that of hRSV-infected A549 cells, with significant expression changes in many of the same immune response genes, including interferon, cytokine, and chemokine signaling pathways (Figs. 4D, E, Supplementary Data 2). Up- and down-regulation of the genes that we identified was consistent across multiple human donor hTBEC samples (Fig. 4D). DEGs from this dataset were used to further narrow our list of DEGs from the WT and Y125A NS1 RNAseq studies in A549 cells.

Based on this strict set of criteria for differential expression in NS1 Y125A versus NS1 WT, hRSV infection, and NS1-MED peaks in all the above comparisons, we identified 143 DEGs and 179 TFs with ChIPseq peaks overlapping with at least one of the DEGs. We next ranked the TFs based on their expression in our RNAseq datasets and the number of DEG targets bound. This ranking revealed activating transcription factor 3 (ATF3) as the top TF, with 140/143 DEG targets and more than 2-fold increased log2 fold change expression with hRSV infection (Figs. 4F, Supplementary Data 3–4).

To experimentally validate that ATF3/chromatin binding coincides with that of NS1/Mediator, we performed Cleavage Under Targets & Release Using Nuclease (CUT&RUN)[38] sequencing of A549 cells expressing hRSV NS1. We used CUT&RUN to map chromatin binding of ATF3, Mediator, and NS1 in A549 cells expressing NS1 or empty vector. CUT&RUN sequencing datasets were analyzed using an adapted pipeline[39,40]. Peaks called in each CUT&RUN dataset were filtered using these criteria: presence in all replicates, total score>100, and not present in empty vector transfected cells. As expected because of the importance of Mediator in controlling the expression of immune response genes[23], the number of Mediator peaks increased 1.6-fold (119,468 to 196,975) with WT NS1 expression compared to empty vector due to the transcriptional response to expression of a viral protein. In NS1-expressing cells, Mediator binding was detected at 1318 DEGs, of which 142 did not have Mediator binding in empty vector cells (Supplementary Data 5). Interferon, chemokine/cytokine, and antigen presentation pathway genes are included in these 142 DEGs. Comparison of NS1 and Mediator chromatin binding revealed that NS1-Mediator overlapping peaks comprised 40% of NS1 peaks (Fig. 4G), which is consistent with our prior ChIP-seq results[17] (43%).

We next evaluated ATF3 chromatin binding profiles. Comparison of ATF3 CUT&RUN in WT NS1 expressing cells revealed 1244 DEGs, of which 118 did not have ATF3 binding in EV cells (Supplementary Data 6). In these the 118, gene pathways included chemokine/cytokine signaling; notably 60% (71/118) were also bound by Mediator. Of NS1-Mediator peaks, 34.5% overlapped with ATF3 peaks (Fig. 4G). Gene annotations of these NS1-Mediator-ATF3 peaks enabled us to link them to 257 DEGs defined in RNAseq from hRSV-infected hTBECs (Figs. 4H, Supplementary Data 7). Many of these NS1/Mediator/ATF3-bound DEGs are involved in immune response to hRSV infection, including interferon signaling (*IFNL2*, *IRF1, STAT1*) (Fig. 4I). Notably, the use of hRSV-infected primary respiratory epithelial cells in these studies enabled detection of differentially expressed immune response pathways that we did not previously identify in cell lines, including chemokine (*CXCL17*), interleukin (*IL18R1*, *IL32*), and Notch (*JAG1*, *JAG2*) (Fig. 4E, I). Together, these new results demonstrate the effects of NS1 expression on Mediator and ATF3 binding to their target genes and reveal a previously unknown role for ATF3 in hRSV infection.

NS1/MED25 ACID complex binds to dsDNA-bound ATF3

We next tested if MED25 directly binds to ATF3 using in vitro pulldown assays. Because ATF3 can bind to many genomic sites and DNA elements[41–43], we recombinantly expressed and purified an MBP-tagged ATF3 basic leucine zipper (bZIP) DNA binding domain in buffer containing either 150 mM NaCl (MBP-ATF3$_{low}$; $A_{260/280}$ = 1.7) or 1 M NaCl (MBP-ATF3$_{high}$; $A_{260/280}$ = 0.63) to dissociate any nonspecific nucleotides from binding to MBP-ATF3. We found that MED25 ACID bound to MBP-ATF3$_{low}$ (Fig. S6A, left panel) and not to MBP-ATF3$_{high}$ (Fig. S6B, left panel), indicating that MED25 ACID binds the nucleotide-bound form of ATF3. In contrast, NS1 does not bind to either MBP-ATF3$_{low}$ or MBP-ATF3$_{high}$ (Fig. S6A, B, middle panels). Addition of the NS1/MED25 ACID complex bound to MBP-ATF3$_{low}$ and not MBP-ATF3$_{high}$ (Figs. S6A, B, right panels), consistent with the results of MED25 ACID alone. To confirm this observation, we also added an exogenous oligonucleotide sequence containing an ATF3 binding site[44] to MBP-ATF3$_{high}$ and recovered binding to MED25 ACID (Fig. 5A, top panel) or NS1/MED25 ACID complex (Fig. 5C, top panel) in in vitro pulldowns but not to NS1 alone (Fig. 5B, top panel). These results demonstrate that both MED25 ACID and the NS1/MED25 ACID complex bind to dsDNA-bound ATF3.

To determine how NS1 binding to MED25 ACID modifies the interaction between MED25 ACID and ATF3, we performed additional

https://doi.org/10.1038/s41467-025-58216-4

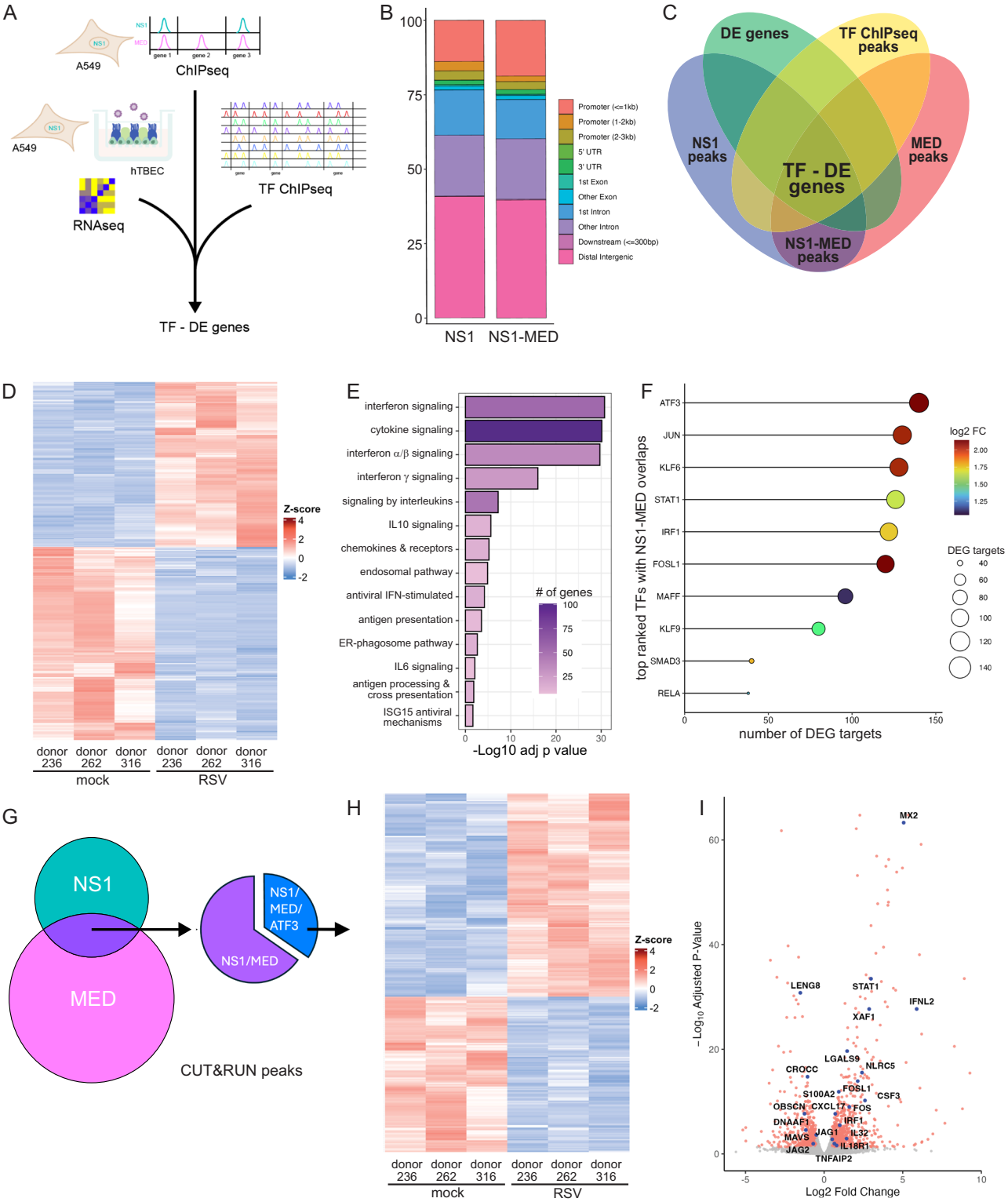

Fig. 4 | ATF3-binding is enriched in genes with NS1-Mediator peaks and differential expression in hRSV infection. A Schematic representation of the integrative analysis that defined overlapping NS1-Mediator ChIPseq peaks from A549 and hTBEC cells transfected with NS1 or empty vector, or infected with hRSV with WT or Y125A mutant NS1; overlapping TF ChIPseq peaks from the ReMap2022 database; and genes bound by these factors that are differentially expressed in cells treated the same as for the NS1-MED ChIPseq. **B** Functional genome annotations of NS1 and NS1-Mediator peaks show an enrichment of proximal promoter binding in the latter compared to the former. **C** Venn diagram representation of the integrative analysis results. **D** Heatmap shows Z-score expression of DEGs in RSV-infected vs mock treated hTBECs [$p_{adj} < 0.05$, log2 FC > abs(1)]. **E** Barplot shows enriched gene pathways in DEGs from (**D**). **F** Lollipop plot shows the number of DEG targets and log2 FC expression of TFs with the highest number of overlapping NS1-Med peaks and DEG targets. **G** Schematic shows the overlap of NS1 and Mediator CUT&RUN peaks and the proportion of those with ATF3 CUT&RUN peak overlaps. **H** Heatmap plotted as in **D** shows DEGs with NS1-Mediator-ATF3 overlapping CUT&RUN peaks. **I** Volcano plot of DEGs in **H** with selected ATF3-bound genes labeled in blue, remainder of DEGs in salmon, and non-DEGs in gray. **D**–**F**, **H**–**I**: padj – FDR adjusted *p* value.

https://doi.org/10.1038/s41467-025-58216-4

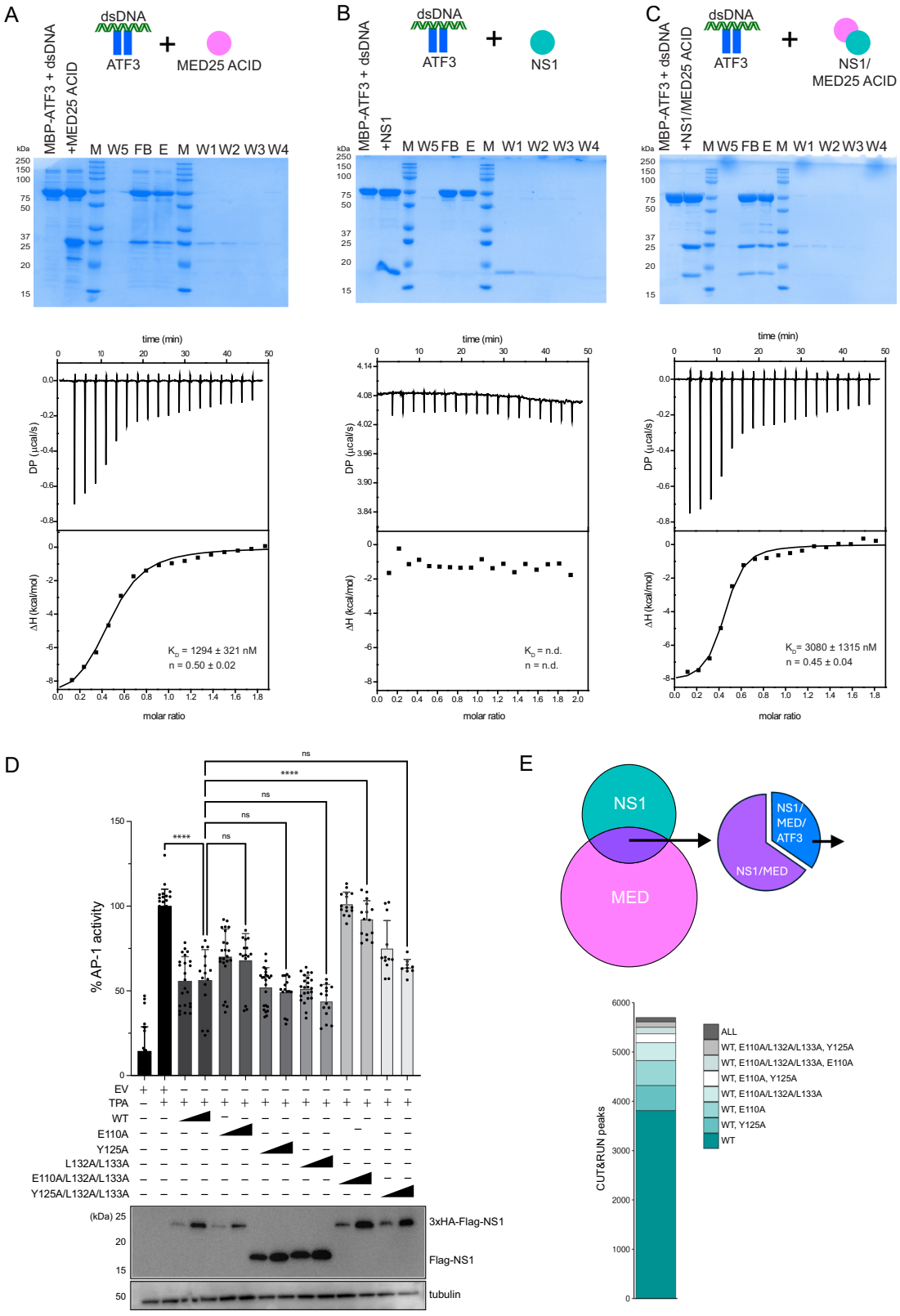

ITC experiments to measure the binding affinities of MED25 ACID and NS1/MED25 ACID complex to dsDNA-bound ATF3. We first determined that ATF3 binds to the dsDNA sequence, 5′-GAGAATTTGCATCATCATTTAG-3′, with a K_D of 94.0 ± 19 nM and an n of 1.0 ± 0.01 (Fig. S6C). We next titrated MED25 ACID into dsDNA-bound ATF3 and measured a K_D of 1294 ± 321 nM with an n of 0.50 ± 0.02, indicating that MED25 ACID binds the ATF3 dimer[45] (Fig. 5A, bottom panel). As a control, we also tested titration of NS1 into dsDNA-bound ATF3 and was not able to measure any heat of binding, consistent with the in vitro pulldown assay results (Fig. 5B, bottom panel). When we added the NS1/MED25 ACID complex, we found that NS1/MED25 ACID complex bound to dsDNA-bound ATF3 with a K_D of 3080 ± 1315 nM. These results demonstrate that NS1 binding to MED25 ACID impacts MED25 interactions with ATF3 by

Fig. 5 | NS1-MED25 ACID complex binds to dsDNA-bound ATF3. Top. In vitro pulldown assays where MBP-ATF3 bZIP proteins purified in high salt conditions (MBP-ATF3$_{high}$) were incubated with excess exogenous dsDNA and immobilized on resin and incubated with **A** MED25 ACID, **B** NS1, and **C** NS1/MED25 ACID complex. M, marker; FB, final beads; E, eluate; W, wash. Bottom. Corresponding ITC assays. A. MED25 ACID, B. NS1, and C. NS1/MED25 ACID complex were titrated into the cell chamber containing dsDNA-bound ATF3 bZIP. Data shown is a representative of three independent experiments. **D** AP-1 luciferase reporter assay. 293 T cells were co-transfected with an AP-1 firefly luciferase reporter plasmid containing the ATF3 binding motif and a constitutively active Renilla luciferase plasmid, along with either empty vector (EV; black) or 100 ng or 250 ng of Flag-tagged NS1 WT, NS1 Y215A, NS1 E110A, or NS1 L132A/L133A (indicated by a gray scale gradient). Twenty-four hours post-transfection, cells were treated with 200 ng/mL TPA for 3 h, and promoter activity was measured as firefly luciferase activity normalized to Renilla luciferase. Results were expressed as a percentage relative to the positive control in the bar graph. Statistical comparisons were performed between NS1 WT and mutant conditions at the same concentration using a one-way ANOVA test. Below the bar graph is a western blot validating protein expression levels for each NS1 construct. Two gels/blots with the same samples were processed in parallel; one blot was probed with anti-Flag antibody and the other blot was probed with anti-Flag and anti-tubulin antibodies. Statistical significance is indicated as follows: not significant (n.s.), $^{*}p < 0.05$, $^{**}p < 0.01$, $^{***}p < 0.001$, and $^{****}p < 0.0001$. **E** Schematic shows the overlap of NS1 and Mediator CUT&RUN peaks and the proportion of those with ATF3 CUT&RUN peak overlaps. Stacked bar graph shows the number of NS1-Mediator-ATF3 overlapping peaks in both replicates (total=5700) in which only WT NS1 binds or the indicated NS1 mutants retain binding.

modestly decreasing the binding affinity of MED25 ACID for ATF3 (Fig. 5C, bottom panel).

We also investigated the functional impact of NS1 WT and NS1 mutants binding on TF binding activity. We used an AP-1 luciferase reporter assay that contains the core binding motif (TGACGTCA) of ATF3[42,43]. We find that 12-O-tetradecanoylphorbol-13-acetate (TPA) stimulation results in an increase in transcriptional activity in the empty vector (EV) control and that NS1 WT expression significantly reduces it (Fig. 5D), which is consistent with our previous results using an IFN-stimulated response element (ISRE) reporter[17]. Expression of NS1 E110A shows reduced impact on transcriptional activity compared to NS1 Y125A or NS1 L132A/L133A. Interestingly, expression of the NS1 triple mutants E110A/L132A/L133A or Y125A/L132A/L133A that do not bind to MED25 results in higher levels of transcriptional activity. These results further support that NS1 binding to Mediator through interactions with MED25 ACID modifies Mediator/TF-directed signaling and transcription.

To test the impact of NS1 mutations on chromatin localization, we performed CUT&RUN sequencing as described above (Fig. 4) and compared binding of NS1 WT and NS1 mutants to NS1/Mediator/ATF3 peaks (5700). Compared to NS1 WT, NS1 Y125A, NS1 E110A, and E110A/L132A/L133A mutants showed a marked decrease in chromatin binding (> 90% reduction, Fig. 5E). Because we detected Mediator binding at more DEGs with NS1 expression compared to empty vector, we next evaluated the impact of NS1 mutants on Mediator bindings. We found that, in mutant NS1 expressing cells, Mediator binds near an additional 341 DEGs compared to Mediator in WT NS1 expressing cells (996 vs 1337). More than 95% of the additional 341 Mediator-bound DEGs are shared across cells expressing each of the mutant NS1 proteins, suggesting that the three mutants have a similar impact. The additional 341 DEGs include genes in interferon response and cytokine signaling pathways, suggesting that mutations that abrogate binding of NS1 to Mediator may allow for Mediator binding and transcriptional regulation of additional immune response genes (Supplementary Data 8). Altogether, these results point to a regulatory role for RSV NS1 in modulating host gene expression through direct interaction with Mediator.

Discussion

Viral control of host gene expression is critical for viral infection, viral propagation, and for viral pathogenesis. The Mediator complex is a target for several viruses because Mediator binds to many TFs and recruits RNA polymerase II to activate transcription of host antiviral genes[28,46]. MED25 is a subunit in the tail module of the Mediator that physically bridges the interaction between transcription factors through the ACID domain and to the rest of the Mediator complex through the VWA domain. Our studies here reveal the first X-ray crystal structure of an RNA viral transcriptional regulator hRSV NS1 bound to MED25 ACID. We also characterize features of this interaction and its functional consequences. Our studies collectively define how viruses may exploit conformational heterogeneity at fuzzy host transcriptional activator interfaces.

The structure of the NS1-MED25 ACID complex shows the similarity of structural folds between NS1 and MED25 ACID, each containing a core β-barrel flanked with α-helices, and that NS1 straddles two sides of MED25 ACID. This two-pronged interaction, one that is driven through electrostatic contacts on one side and the other through hydrophobic contacts on the other side, had been previously observed in the binding between MED25 ACID to herpes simplex virus VP16 protein[24,25]. The interfaces of MED25 ACID that bind to NS1 and VP16 are generally similar. For VP16 binding to the electrostatic "H2 face", MED25 ACID Gln451 and Arg466 are critical as charge reversal mutations of these residues result in a loss of binding to MED25 ACID[24,25]. For NS1 binding, MED25 ACID Arg466 contributes to binding, but we find additional important contributions from Ser516, Ser517, Lys518, and Lys519 that anchor binding to NS1 Glu110 and Lys112 (Figs. 4 and Table S1). Mutation of NS1 Gln110 results in a significant loss of binding to MED25 ACID and addition of mutation of Tyr125 or Leu132/Leu133 on the NS1 α3 helix leads to complete loss of binding. The residues that comprise the MED25 ACID hydrophobic "H1 face" and that are important for VP16 binding are also critical for NS1 binding. The dynamic C-terminal NS1 α3 helix that was previously shown to be critical for NS1 IFN antagonist function[16,17] binds in the MED25 ACID hydrophobic groove. Mutation of NS1 Tyr125, Leu132, and Leu133 residues results in loss of binding to MED25. While our studies were in progress, another study also showed that the NS1 α3 helix bound to the "H2 face" of MED25 ACID. However, this study was limited to NMR analysis of MED25 ACID binding to the NS1 α3 helix peptide, which is likely unstructured in the absence of the full-length NS1 protein as evidenced by the low binding affinity[29]. Furthermore, mutational analysis of MED25 ACID did not fully corroborate their description of the NS1 α3 helix binding interface. Our structure and biochemical analysis described in this study clearly reveals the importance of the full-length NS1 protein and how critical contacts at two NS1 regions are required for driving interactions with MED25 ACID.

While several MED25 residues overlap with those that facilitate binding to hRSV NS1 and HSV VP16, we observed distinct electrostatic contacts in our structure. Given that HSV is a DNA virus and hRSV is an RNA virus, these differences may also inform on the replication kinetics as well as the differences of host factors for viruses that replicate at distinct subcellular locations. This is consistent with the structural flexibility observed of MED25 ACID and of Mediator subunits that bind to many TFs with varying sequences[21,23,28]. The fuzzy nature of these interactions mediated through multiple contacts at protein-protein interfaces is what allows for overall high affinity binding and accommodates specific binding to different protein partners[47–49]. Given the similarly of structures observed for NS1 and MED25 ACID, it is interesting to speculate that the same conformational plasticity observed in MED25 ACID is likely present in NS1 in its ability to target different host molecules. In studies here, we find that the NS1 linker and α3 helix are conformationally dynamic and that the α3 helix participates in critical interfacial interactions with MED25 ACID that are different from NS1 alone. Additional studies of NS1 with other

interactors warrants further exploration. We note that a prior study, using NMR chemical shift mapping, reported an α3 helix peptide interaction on MED25 ACID[29]. A large number of residues were identified in that report and those residues spanned large surfaces of the MED25 ACID domain. Of note, several key residues including MED25 ACID residues Ser468, Met470, and Met523 were predicted to be at the interface, but they are not at the binding interfaces defined in our X-ray crystal structure.

Transcriptional regulation of immune response genes is an essential aspect of innate host defense against viral infection. Most transcriptional regulation studies focus on the role of host TFs in the cytoplasm or non-nuclear organelles by sensors of viral infection. Earlier work on hRSV NS1 demonstrated immune evasion through interference with RIG-I activation or its interaction with MAVS, suppressing activation of IRF TFs, or enhancing the degradation of STAT family members[50–54]. Our recent studies demonstrate that hRSV NS1 localizes to the nucleus of primary human respiratory epithelial cells and cell lines and binds chromatin at sites overlapping with Mediator in regulatory regions near viral response genes[16,17]. Here, our unbiased examination of chromatin binding by NS1-Mediator and TFs as well as gene expression datasets revealed a striking enrichment for TF ATF3 binding at genes whose expression was significantly altered by hRSV infection and the NS1 Y125A mutation. Our CUT&RUN studies using NS1 WT and NS1 Y125A, E110A, and E110A/L132A/L133A mutants confirmed that ATF3 binds at one-third of NS1-Mediator sites, including many immune response genes that are differentially expressed in hRSV infection. RNAseq of hRSV-infected primary respiratory epithelial cells in these studies enabled detection of NS1-Mediator-ATF3 bound DEGs in immune response pathways that we did not previously identify in cell lines, including Notch signaling genes *JAG1* and *JAG2*. JAG1 and JAG2 regulate cell fate determination in hTBECs and JAG1 promotes the differentiation of Th2 lymphocytes in RSV infection[55,56]. These findings support a role for NS1/Mediator/ATF3 interaction in modulation of host gene regulation in hRSV infection, including innate and adaptive immune response pathways.

ATF3 is a member of the AP-1 family of TFs that is well described in its role as a stress-induced transcription factor that regulates cell growth, apoptosis, and inflammatory responses[41–43]. ATF3 also regulates pathways involved in metabolism, immunity, and oncogenesis[57–60]. ATF3 expression is increased in a range of pulmonary infections and inflammatory diseases, including acute lung injury/acute respiratory distress disorder and bacterial pneumonia. In these conditions, it was shown to play a protective role by regulating expression of pro-inflammatory pathways and promoting proliferation and recovery of lung epithelium[61–64]. More recently, ATF3 has been identified as critical in the immune responses to RNA viral infections[41]. Notably, ATF3 has not been previously recognized as playing a role in hRSV infection or as part of an interaction with NS1. Our studies here indicate a broader role for ATF3 in response to hRSV NS1 localization to Mediator. ATF3 can also heterodimerize with other AP-1 family members, including JUN[65,66]. Interestingly, our analyzes identified JUN as highly ranked by chromatin binding at NS1-Mediator sites, total DEG targets, and its own differential expression. *JUN* family members are immediate early genes induced upon a variety of stimuli, including cellular stress; their protein products regulate a diverse set of processes including cell proliferation, differentiation, apoptosis, and oncogenesis[67]. Further study is needed to determine whether NS1/MED25 interactions involve heterodimers of ATF3 with other AP-1 family members in binding chromatin and to probe the overall role of ATF3 in gene regulation of immune responses during hRSV infection.

Collectively, our results here provide molecular insights into a viral transcriptional regulator from human respiratory syncytial virus NS1 and its specific interactions with MED25 of Mediator complex. NS1 mimics the structural fold present in MED25 ACID to target MED25 and ATF3-associated genes. Interestingly, binding of NS1 to MED25 ACID does not drastically impact the binding affinity of MED25 ACID to dsDNA-bound ATF3. This result hints at the possibility that NS1 binding may instead induce a different consequence in the overall conformation of MED25/ATF3 that enables or dampens transcription signals. Understanding the arrangement of this complex will provide additional insight into viral gene regulatory mechanisms and reveal targets that can facilitate development of therapeutic strategies for hRSV infections. These results further highlight how conformational heterogeneity at host interfaces are continually exploited by viruses.

Methods

Cloning, expression, and purification of recombinant proteins

hRSV NS1 (1-139), hMED25 ACID (389-543), hATF3 (1-181) or hATF3 bZIP (88-149) residues were subcloned into modified pET15b containing a tandem maltose binding protein (MBP) and His_6 tag as fusion partners and pACYC vectors (Novagen). hMED25 VWA was subcloned into a modified pGEX vector (GE Healthcare). All constructs, including mutants, were verified by Sanger sequencing. Plasmid vectors were transformed into *Escherichia coli* strain BL21(DE3) and grown in Luria-Bertani medium containing antibiotics at 37 °C to an optical density (A_{600}) of 0.6–0.7. Protein expression was induced with 0.5 mM isopropyl β-D-1-thiogalactopyranoside (IPTG) for 14 h at 18 °C. Cells were harvested by centrifugation at 30,000 × *g* and frozen in liquid nitrogen. Cells expressing NS1 or MED25 ACID were lysed using an Emulsiflex-C5 homogenizer (Avestin) and clarified by centrifugation at 69,673 × *g*. Proteins were purified using a series of affinity and ion exchange chromatographic columns followed by a Superdex 75 16/60 column (Cytiva) in buffer containing 20 mM Tris pH 8.0, 150 mM NaCl, and 2 mM tris(2-carboxyethyl) phosphine (TCEP). Recombinantly expressed MBP-ATF3 or ATF3 bZIP was either lysed in low salt conditions (MBP-$ATF3_{low}$/ATF3 $bZIP_{low}$; 25 mM phosphate buffer, pH 7, 150 mM NaCl, 20 mM imidazole, 5 mM bME) or high salt conditions (MBP-$ATF3_{high}$/ATF3 $bZIP_{high}$; 25 mM phosphate buffer, pH 7, 1 M NaCl, 20 mM imidazole, 5 mM bME) prior to purification on a Ni6 fast flow column (Cytiva). Purity of the protein was assessed by Coomassie blue staining of SDS-PAGE.

In vitro pull-down assays

Amylose resin (for MBP-tagged proteins) (New England Biolabs) or glutathione sepharose resin (for GST-tagged proteins) (Cytiva) was pre-equilibrated with buffer containing 20 mM Tris pH 8.0, 150 mM NaCl, and 5 mM bME or 25 mM phosphate buffer, pH 7.0 and 150 mM or 1 M NaCl, 2 mM TCEP. Purified MBP or GST tagged proteins (100 mg) were immobilized on resin prior to the addition of a protein binding partner (100 mg) and incubated at 25 °C for 5 min. Unbound material was discarded and the resin was washed five times with the equilibration buffer. Protein(s) was eluted from the resin in buffer containing 1% maltose (Sigma-Aldrich) for MBP-bound or 10 mM glutathione (reduced) (Sigma-Aldrich) for GST-bound proteins. Oligonucleotides encoding the ATF3 binding promoter sequences (5′-CATGTGGCTTGATGCAAACCTGGAGAAT**TTGCATCA**TCATTTAGC-3′)[44] and (5′-GAGAAT**TTGCATCA**TCATTTAG-3′) were obtained from Integrated DNA Technologies and annealed prior to incubation with MBP-$ATF3_{high}$/ATF3 $bZIP_{high}$. Samples were collected at each step of the assay for analysis by Coomassie blue staining of SDS-PAGE.

Isothermal titration calorimetry studies

All proteins were dialyzed in 20 mM Tris, pH 8.0 and 150 mM NaCl overnight at 4 °C or in 25 mM phosphate buffer, pH 7.0 and 250 mM NaCl, 2 mM TCEP (for binding experiments with ATF3). Isothermal titration calorimetry (ITC) titrations were performed using a PEAQ-isothermal titration calorimeter (Malvern) at 25 °C. hMED25 ACID or hMED25ACID/NS1 proteins were loaded into the injection syringe and hRSV NS1 or ATF3 $bZIP_{high}$ (with dsDNA) protein into the cell chamber.

Calorimetric data were fitted into a single-binding site model with a 1:1 stoichiometry and were processed using Origin software (OriginLab).

Size exclusion chromatography-multiangle light scattering (SEC-MALS) analysis

SEC-MALS experiments were carried out in buffer containing 20 mM Tris (pH 8.0), 150 mM NaCl, and 2 mM TCEP with a sample concentration of 2 mg/mL and using a DAWN-HELEOS II detector (Wyatt Technologies) coupled to a Superdex 75 Increase 5/150 GL column (Cytiva). Acquired data from UV, MALS, and RI detectors were analyzed to determine the weight-averaged molecular mass (Mw) of the proteins using ASTRA 6 software (Wyatt Technologies). Protein concentrations were determined using the refractive index measured by an Optilab T-rEX (Wyatt Technologies) using a dn/dc = 0.185 mL^3/g.

Thermal shift assay

A 10 μM protein (NS1 and MED25 ACID proteins) stock and a 10X stock of SYPRO Orange Protein Gel Stain (S6650, Thermo Fisher Scientific) were prepared in 20 mM Tris, pH 8.0 buffer. Protein (5 μM) and the dye (5X) were finally added to the wells of a 96-well plate (MicroAmp™ EnduraPlate™ Optical 96-Well Clear Reaction Plates with Barcode, Thermo Fisher Scientific, 4483354) and plates were sealed with MicroAmp™ Optical Adhesive Film (Thermo Fisher Scientific, 4360954). Plates were placed in a QuantStudio5 qRT-PCR machine (Applied Biosystems by Thermo Fisher Scientific) which was programmed to cool the block to 20 °C at 3.1 °C/s, hold the block at 20 °C for 1 min followed by ramping up from 20–95 °C at 0.05 °C/s and fluorescence was recorded at or near 570 nm. Thermal shift data was acquired in the Protein Thermal Shift Software 1.4 (Applied Biosystems) and analyzed in GraphPad Prism by plotting fluorescence counts versus temperature for each condition and graphs were prepared using Origin software (OriginLab).

Hydrogen-deuterium exchange-mass spectrometry (HDX-MS) studies

hRSV NS1 was buffer exchanged into PBS buffer (pH 7.4). NS1 was diluted with PBS buffer in D_2O (pH 7.0, pD 7.4) to initiate deuterium labeling, or with PBS buffer in H_2O for peptide mapping or for a no deuterium control. At different time intervals (10, 60, 120, 900, 3600, 14400 s), the HDX reaction was quenched via a 2:3 dilution with 3 M urea (final pH 2.5) at 4 °C. The sample was injected into a custom built HDX setup to be digested on an in-house coupled and packed immobilized pepsin column, trapped and desalted on a ZORBAX Eclipse XDB C8 column (2.1 mm × 15 mm, Agilent) using water/0.1% trifluoroacetic acid, analytically separated on a Hypersil Gold C18 column (2.1 mm × 50 mm, Thermo Fisher) using a gradient from 4 to 40% acetonitrile/0.1% formic acid, and eluted into a LTQ-FTICR mass spectrometer (Thermo Fisher) for MS/MS (peptide mapping) or MS (HDX) analysis. All valves, tubes, and columns (except for the pepsin column) were submerged in an ice-water bath to minimize back-exchange. Peptide mapping data were analyzed using Byos (Protein Metrics Inc.), and HDX data were analyzed using HDExaminer (Sierra Analytics).

Protein crystallization, data collection, and structure determination

Initial crystallization experiments were carried out using commercially available screens (Hampton Research). Initial hits were subsequently optimized using in-house generated reagents and the hanging-drop vapor-diffusion method at 20 °C to obtain diffraction quality crystals. Single crystals were harvested and cryo-cooled in liquid nitrogen. X-ray diffraction datasets were collected at the Advanced Light Source (Beamline 8.2.2, Advanced Light Source, Berkeley, CA) at 100 K. X-Ray detector software (XDS) was used to index, process, and scale all data sets automatically[68], followed by reprocessing with HKL3000[69] to assess data information content. The NS1-MED25 ACID complex structure was solved using the CCP4i2 suite of programs[70]. CCP4mg was used to generate an ensemble of hMED25 ACID structure (PDB ID 2L23) that was used along with the crystal structure of NS1 (PDB ID 5VJ2) as templates for molecular replacement using PhaserMR[71]. The structure was subjected to several rounds of refinement using REFMAC[72] and after each step of refinement, the electron-density maps were manually inspected and modified in Coot[73]. The quality of the atomic model was assessed with Molprobity[74]. AREAiMOL and PISA were used for solvent accessible surface area calculation and protein interface determination, respectively[75,76]. The final structure was rendered using PyMOL (Version 3.0 Schrödinger, LLC.). The crystal parameters and data-processing statistics are summarized in Supplementary Table 1 (Table S1).

AP-1 luciferase reporter assay

AP-1 reporter assays were performed in HEK 293 T cells using 200 ng of an AP-1 promoter-firefly luciferase reporter plasmid (pGL4.44[luc2P/AP1 RE/Hygro] Vector, Promega) and 20 ng of a constitutively expressed Renilla luciferase reporter plasmid. Cells were co-transfected with NS1 WT or mutants at concentrations indicated in the figure legends. Transfections were carried out in suspension using Lipofectamine 2000 and OptiMEM following the manufacturer's protocol. 24 h post-transfection, AP-1 activity was induced with 100–200 ng/mL TPA (12-O-Tetradecanoylphorbol-13-Acetate) for 3 h. Cells were harvested, and luciferase activity was measured using the Dual-Luciferase Reporter Assay System (Promega). Firefly luciferase activity was normalized to Renilla luciferase activity, and the results are presented relative to AP-1 activity in EV-transfected cells, which was set to 100. Data analysis and graph generation were performed using GraphPad Prism. Error bars represent the standard deviation of at least three independent experiments, each performed in technical triplicates.

In vitro viral infections

Human tracheobronchial epithelial cells (hTBECs) were obtained as surgical excess from lung donated for transplant as anonymized and exempt from regulation by HHS regulation 45 CFR Part 46. Cells were differentiated on Transwell membranes (Corning) using air-liquid interface conditions consisting of basal, secretory, and multiciliated cells as described[77,78]. Fully differentiated cultures on Transwells were infected with hRSV strain A2 (ATCC) at MOI of 3. Phosphate buffered saline (PBS) was used for the mock infections. At 2 h post infection (hpi), the virus was removed by aspiration and cells were washed three times with PBS followed by incubation at 37 °C for 72 h. After 72 hpi, cells were harvested, and RNA extraction was performed using QIAGEN RNA Easy kit.

CUT&RUN-, ChIP-, and RNA-sequencing

RNA-seq of RNA extracted from mock or hRSV infected hTBECs from 3 donors was performed by the WU GTAC@MGI using Takara Bio SMARTer cDNA synthesis followed by library preparation according to manufacturer's protocol (Takara), indexed, pooled, and sequenced (2 × 150 bp PE reads) on an Illumina NovaSeq X instrument according to the manufacturer's instruction. CUT&RUN sequencing of 0.5×10^6 A549 cells transfected with empty vector, WT, or mutant NS1 plasmids was performed using the following antibodies: anti-HA tag (Epycypher), anti-MED1 (Bethyl Lab), and anti-ATF3 (D2Y5W) and the ChIC/CUT&RUN kit V4 (EpiCypher Cutana) according to the manufacturer's instructions. CUT&RUN libraries were prepared using CUT&RUN library Prep Kit V1.5 (Epycypher). Integrity and concentrations of the final libraries were examined by electrogram obtained on Tape Station 4150 (Agilent). The indexed libraries (16 ng of each) were pooled and sequenced (2 × 150 bp PE reads) on an Illumina NovaSeq X instrument. ChIP-seq of NS1 and Mediator in A549 cells infected with hRSV or

mock-infected, or transfected with WT or Y125A NS1, were previously reported[17]. Bulk RNA-seq datasets from A549 cells infected with WT or Y125A NS1 hRSV were previously reported[16,17].

CUT&RUN-, ChIP-, and RNA-sequencing integrative analysis

CUT&RUN fastq files were aligned and analyzed using a pipeline adapted from[39,40] using bowtie2, samtools, bedtools, and SEACR[79,80] with default parameters. Peaks were filtered using these criteria: presence in all replicates, total score>100, and not present in empty vector anti-HA. Genome annotation of peaks to assign genome functional classification and nearest gene was performed with ChIPseeker[81]. Gene annotations of peaks were used to link CUT&RUN peaks to DEGs defined in RNAseq from transfected A549 and infected hTBECs. Alignment and peak calling analysis of NS1 and Mediator ChIP-seq was previously reported17. TF peaks overlapping NS1 and Mediator peaks were identified using the ReMapEnrich R software package (https://github.com/remap-cisreg/ReMapEnrich) and the most recent and comprehensive catalog of publicly available human factor ChIP-seq data43. Analysis of RNA-seq from hTBECs was performed as follows. Basecalling and demultiplexing were performed with Illumina's bcl2fastq software and a custom python demultiplexing program with a maximum of one mismatch in the indexing read allowed. RNA-seq reads were then aligned to the Ensembl release 101 primary assembly with STAR version 2.7.9a44. Gene counts were obtained from the number of uniquely aligned unambiguous reads by Subread:featureCount version 2.0.345. Isoform expression of known Ensembl transcripts were quantified with Salmon version 1.5.246. Sequencing performance was assessed for the total number of aligned reads, total number of uniquely aligned reads, and features detected. Ribosomal genes and genes not expressed in the smallest group size minus one sample greater than one count-per-million were excluded from further analysis. All RNAseq datasets were imported and normalized using estimateSizeFactors and indicated conditions were compared using DESeq2 R package version 1.45.047 to define DEGs using FDR q value < 0.05. DEG targets and TFs were required to have a baseMean>100 using normalized DESeq2 values. Statistical analyzes, filtering, and data visualization were performed using R software (v4.4.2).

Reporting summary

Further information on research design is available in the Nature Portfolio Reporting Summary linked to this article.

Data availability

The NS1-MED25 ACID crystal structure and reflection data are available in the Protein Data Bank under PDB 9CCV (https://www.rcsb.org/). Sequencing data are available in NCBI GEO under the accession numbers GSE155152, GSE270463, and GSE99298. Mass spectrometry data are available via ProteomeXchange under the identifier PXD054004 and PXD054005 (https://www.proteomexchange.org/). Source data are provided as a Source Data file. Key reagents and resources are provided in Supplementary Data 9. Source data are provided with this paper.

References

1. McLaughlin, J. M. et al. Respiratory syncytial virus-associated hospitalization rates among US infants: a systematic review and meta-analysis. *J. Infect. Dis.* **225**, 1100–1111 (2022).
2. Rha, B. et al. Respiratory syncytial virus-associated hospitalizations among young children: 2015–2016. *Pediatrics* **146**, e20193611 (2020).
3. Branche, A. R. et al. Incidence of respiratory syncytial virus infection among hospitalized adults, 2017–2020. *Clin. Infect. Dis.* **74**, 1004–1011 (2022).
4. Hansen, C. L., Chaves, S. S., Demont, C. & Viboud, C. Mortality associated with influenza and respiratory syncytial virus in the US, 1999–2018. *JAMA Netw. Open* **5**, e220527 (2022).
5. Matias, G. et al. Estimates of mortality attributable to influenza and RSV in the United States during 1997–2009 by influenza type or subtype, age, cause of death, and risk status. *Influenza Other Respir. Viruses* **8**, 507–515 (2014).
6. Thompson, W. W. et al. Mortality associated with influenza and respiratory syncytial virus in the United States. *JAMA* **289**, 179–186 (2003).
7. Papi, A. et al. Respiratory syncytial virus prefusion f protein vaccine in older adults. *N. Engl. J. Med* **388**, 595–608 (2023).
8. Walsh, E. E. et al. Efficacy and safety of a bivalent RSV prefusion F vaccine in older adults. *N. Engl. J. Med* **388**, 1465–1477 (2023).
9. Wilson, E. et al. Efficacy and safety of an mRNA-based RSV PreF vaccine in older adults. *N. Engl. J. Med* **389**, 2233–2244 (2023).
10. Kampmann, B. et al. Bivalent prefusion F vaccine in pregnancy to prevent RSV illness in infants. *N. Engl. J. Med* **388**, 1451–1464 (2023).
11. Agac, A. et al. Host responses to respiratory syncytial virus infection. *Viruses* **15**, 1999 (2023).
12. Howley, P. M. & Knipe, D. M. *Fields virology*, volumes (Wolters Kluwer, Philadelphia, 2021).
13. Merritt, T. N., Pei, J. & Leung, D. W. Pathogenicity and virulence of human respiratory syncytial virus: Multifunctional nonstructural proteins NS1 and NS2. *Virulence* **15**, 2283897 (2023).
14. Spann, K. M., Tran, K. C., Chi, B., Rabin, R. L. & Collins, P. L. Suppression of the induction of alpha, beta, and lambda interferons by the NS1 and NS2 proteins of human respiratory syncytial virus in human epithelial cells and macrophages [corrected]. *J. Virol.* **78**, 4363–4369 (2004).
15. Lo, M. S., Brazas, R. M. & Holtzman, M. J. Respiratory syncytial virus nonstructural proteins NS1 and NS2 mediate inhibition of Stat2 expression and alpha/beta interferon responsiveness. *J. Virol.* **79**, 9315–9319 (2005).
16. Chatterjee, S. et al. Structural basis for human respiratory syncytial virus NS1-mediated modulation of host responses. *Nat. Microbiol* **2**, 17101 (2017).
17. Pei, J. et al. Nuclear-localized human respiratory syncytial virus NS1 protein modulates host gene transcription. *Cell Rep.* **37**, 109803 (2021).
18. Swedan, S., Andrews, J., Majumdar, T., Musiyenko, A. & Barik, S. Multiple functional domains and complexes of the two nonstructural proteins of human respiratory syncytial virus contribute to interferon suppression and cellular location. *J. Virol.* **85**, 10090–10100 (2011).
19. Van Royen, T. et al. An unexpected encounter: respiratory syncytial virus nonstructural protein 1 interacts with mediator subunit MED25. *J. Virol.* **96**, e0129722 (2022).
20. Wu, W. et al. The interactome of the human respiratory syncytial virus NS1 protein highlights multiple effects on host cell biology. *J. Virol.* **86**, 7777–7789 (2012).
21. Richter, W. F., Nayak, S., Iwasa, J. & Taatjes, D. J. The Mediator complex as a master regulator of transcription by RNA polymerase II. *Nat. Rev. Mol. Cell Biol.* **23**, 732–749 (2022).
22. Kornberg, R. D. Mediator and the mechanism of transcriptional activation. *Trends Biochem Sci.* **30**, 235–239 (2005).
23. Soutourina, J. Transcription regulation by the Mediator complex. *Nat. Rev. Mol. Cell Biol.* **19**, 262–274 (2018).
24. Milbradt, A. G. et al. Structure of the VP16 transactivator target in the Mediator. *Nat. Struct. Mol. Biol.* **18**, 410–415 (2011).
25. Vojnic, E. et al. Structure and VP16 binding of the Mediator Med25 activator interaction domain. *Nat. Struct. Mol. Biol.* **18**, 404–409 (2011).
26. Yamamoto, S., Eletsky, A., Szyperski, T., Hay, J. & Ruyechan, W. T. Analysis of the varicella-zoster virus IE62 N-terminal acidic

transactivating domain and its interaction with the human mediator complex. *J. Virol.* **83**, 6300–6305 (2009).
27. Yang, M., Hay, J. & Ruyechan, W. T. Varicella-zoster virus IE62 protein utilizes the human mediator complex in promoter activation. *J. Virol.* **82**, 12154–12163 (2008).
28. Rovnak, J. & Quackenbush, S. L. Exploitation of the Mediator complex by viruses. *PLoS Pathog.* **18**, e1010422 (2022).
29. Dong, J. et al. Respiratory syncytial virus NS1 protein targets the transactivator binding domain of MED25. *J. Mol. Biol.* **434**, 167763 (2022).
30. Abdella, R. et al. Structure of the human Mediator-bound transcription preinitiation complex. *Science* **372**, 52–56 (2021).
31. Rengachari, S., Schilbach, S., Aibara, S., Dienemann, C. & Cramer, P. Structure of the human Mediator-RNA polymerase II pre-initiation complex. *Nature* **594**, 129–133 (2021).
32. Money, V. A., McPhee, H. K., Mosely, J. A., Sanderson, J. M. & Yeo, R. P. Surface features of a Mononegavirales matrix protein indicate sites of membrane interaction. *Proc. Natl Acad. Sci. USA* **106**, 4441–4446 (2009).
33. Bontems, F. et al. NMR structure of the human Mediator MED25 ACID domain. *J. Struct. Biol.* **174**, 245–251 (2011).
34. Eletsky, A. et al. Solution NMR structure of MED25(391–543) comprising the activator-interacting domain (ACID) of human mediator subunit 25. *J. Struct. Funct. Genomics* **12**, 159–166 (2011).
35. Krissinel, E. Enhanced fold recognition using efficient short fragment clustering. *J. Mol. Biochem* **1**, 76–85 (2012).
36. Lawrence, M. C. & Colman, P. M. Shape complementarity at protein/protein interfaces. *J. Mol. Biol.* **234**, 946–950 (1993).
37. Hammal, F., de Langen, P., Bergon, A., Lopez, F. & Ballester, B. ReMap 2022: a database of human, mouse, drosophila and Arabidopsis regulatory regions from an integrative analysis of DNA-binding sequencing experiments. *Nucleic Acids Res.* **50**, D316–D325 (2022).
38. Skene, P. J. & Henikoff, S. An efficient targeted nuclease strategy for high-resolution mapping of DNA binding sites. *Elife* **6**, e21856 (2017).
39. Meers, M. P., Bryson, T. D., Henikoff, J. G. & Henikoff, S. Improved CUT&RUN chromatin profiling tools. *Elife* **8**, e46314 (2019).
40. Meers, M. P., Tenenbaum, D. & Henikoff, S. Peak calling by sparse enrichment analysis for CUT&RUN chromatin profiling. *Epigenetics Chromatin* **12**, 42 (2019).
41. Liu, S. et al. The dual roles of activating transcription factor 3 (ATF3) in inflammation, apoptosis, ferroptosis, and pathogen infection responses. *Int J. Mol. Sci.* **25**, 824 (2024).
42. Wolfgang, C. D., Liang, G., Okamoto, Y., Allen, A. E. & Hai, T. Transcriptional autorepression of the stress-inducible gene ATF3. *J. Biol. Chem.* **275**, 16865–16870 (2000).
43. Zhao, J., Li, X., Guo, M., Yu, J. & Yan, C. The common stress responsive transcription factor ATF3 binds genomic sites enriched with p300 and H3K27ac for transcriptional regulation. *BMC Genomics* **17**, 335 (2016).
44. Wang, L. et al. ATF3 promotes erastin-induced ferroptosis by suppressing system Xc(). *Cell Death Differ.* **27**, 662–675 (2020).
45. Chen, B. P., Wolfgang, C. D. & Hai, T. Analysis of ATF3, a transcription factor induced by physiological stresses and modulated by gadd153/Chop10. *Mol. Cell Biol.* **16**, 1157–1168 (1996).
46. Liu, X. et al. Human virus transcriptional regulators. *Cell* **182**, 24–37 (2020).
47. Fuxreiter, M. Electrostatics tunes protein interactions to context. *Proc. Natl Acad. Sci. USA* **119**, e2209201119 (2022).
48. Sanborn, A. L. et al. Simple biochemical features underlie transcriptional activation domain diversity and dynamic, fuzzy binding to Mediator. *Elife* **10**, e68068 (2021).
49. Schreiber, G. & Keating, A. E. Protein binding specificity versus promiscuity. *Curr. Opin. Struct. Biol.* **21**, 50–61 (2011).
50. Ban, J. et al. Human respiratory syncytial virus NS 1 Targets TRIM25 to suppress RIG-I ubiquitination and subsequent RIG-I-mediated antiviral signaling. *Viruses* **10**, 716 (2018).
51. Boyapalle, S. et al. Respiratory syncytial virus NS1 protein colocalizes with mitochondrial antiviral signaling protein MAVS following infection. *PLoS One* **7**, e29386 (2012).
52. Goswami, R. et al. Viral degradasome hijacks mitochondria to suppress innate immunity. *Cell Res* **23**, 1025–1042 (2013).
53. Spann, K. M., Tran, K. C. & Collins, P. L. Effects of nonstructural proteins NS1 and NS2 of human respiratory syncytial virus on interferon regulatory factor 3, NF-kappaB, and proinflammatory cytokines. *J. Virol.* **79**, 5353–5362 (2005).
54. Swedan, S., Musiyenko, A. & Barik, S. Respiratory syncytial virus nonstructural proteins decrease levels of multiple members of the cellular interferon pathways. *J. Virol.* **83**, 9682–9693 (2009).
55. Qin, L. et al. Bronchial epithelial cells promote the differentiation of Th2 lymphocytes in airway microenvironment through jagged/notch-1 signaling after RSV infection. *Int Arch. Allergy Immunol.* **179**, 43–52 (2019).
56. Reynolds, S. D. et al. Assemblies of JAG1 and JAG2 determine tracheobronchial cell fate in mucosecretory lung disease. *JCI Insight* **7**, e157380 (2022).
57. Hai, T., Wolford, C. C. & Chang, Y. S. ATF3, a hub of the cellular adaptive-response network, in the pathogenesis of diseases: is modulation of inflammation a unifying component? *Gene Expr.* **15**, 1–11 (2010).
58. Ku, H. C. & Cheng, C. F. Master regulator activating transcription factor 3 (ATF3) in metabolic homeostasis and cancer. *Front Endocrinol. (Lausanne)* **11**, 556 (2020).
59. Thompson, M. R., Xu, D. & Williams, B. R. ATF3 transcription factor and its emerging roles in immunity and cancer. *J. Mol. Med (Berl.)* **87**, 1053–1060 (2009).
60. van Dam, H. & Castellazzi, M. Distinct roles of Jun: Fos and Jun: ATF dimers in oncogenesis. *Oncogene* **20**, 2453–2464 (2001).
61. Ali, M. et al. Transcriptional responses to injury of regenerative lung alveolar epithelium. *iScience* **25**, 104843 (2022).
62. Kwon, J. W. et al. Activating transcription factor 3 represses inflammatory responses by binding to the p65 subunit of NF-kappaB. *Sci. Rep.* **5**, 14470 (2015).
63. Nguyen, C. T., Kim, E. H., Luong, T. T., Pyo, S. & Rhee, D. K. ATF3 confers resistance to pneumococcal infection through positive regulation of cytokine production. *J. Infect. Dis.* **210**, 1745–1754 (2014).
64. Qian, L., Zhao, Y., Guo, L., Li, S. & Wu, X. Activating transcription factor 3 (ATF3) protects against lipopolysaccharide-induced acute lung injury via inhibiting the expression of TL1A. *J. Cell Physiol.* **232**, 3727–3734 (2017).
65. Hai, T., Wolfgang, C. D., Marsee, D. K., Allen, A. E. & Sivaprasad, U. ATF3 and stress responses. *Gene Expr.* **7**, 321–335 (1999).
66. Liang, G., Wolfgang, C. D., Chen, B. P., Chen, T. H. & Hai, T. ATF3 gene. genomic organization, promoter, and regulation. *J. Biol. Chem.* **271**, 1695–1701 (1996).
67. Chinenov, Y. & Kerppola, T. K. Close encounters of many kinds: Fos-Jun interactions that mediate transcription regulatory specificity. *Oncogene* **20**, 2438–2452 (2001).
68. Kabsch, W. Xds. *Acta Crystallogr D. Biol. Crystallogr* **66**, 125–132 (2010).
69. Otwinowski, Z. & Minor, W. Processing of X-ray diffraction data collected in oscillation mode. *Methods Enzymol.* **276**, 307–326 (1997).
70. Agirre, J. et al. The CCP4 suite: integrative software for macromolecular crystallography. *Acta Crystallogr D. Struct. Biol.* **79**, 449–461 (2023).
71. McCoy, A. J. et al. Phaser crystallographic software. *J. Appl Crystallogr* **40**, 658–674 (2007).

72. Murshudov, G. N., Vagin, A. A. & Dodson, E. J. Refinement of macromolecular structures by the maximum-likelihood method. *Acta Crystallogr D. Biol. Crystallogr* **53**, 240–255 (1997).
73. Emsley, P., Lohkamp, B., Scott, W. G. & Cowtan, K. Features and development of Coot. *Acta Crystallogr D. Biol. Crystallogr* **66**, 486–501 (2010).
74. Chen, V. B. et al. MolProbity: all-atom structure validation for macromolecular crystallography. *Acta Crystallogr D. Biol. Crystallogr* **66**, 12–21 (2010).
75. Krissinel, E. & Henrick, K. Inference of macromolecular assemblies from crystalline state. *J. Mol. Biol.* **372**, 774–797 (2007).
76. Lee, B. & Richards, F. M. The interpretation of protein structures: estimation of static accessibility. *J. Mol. Biol.* **55**, 379–400 (1971).
77. Horani, A., Nath, A., Wasserman, M. G., Huang, T. & Brody, S. L. Rho-associated protein kinase inhibition enhances airway epithelial Basal-cell proliferation and lentivirus transduction. *Am. J. Respir. Cell Mol. Biol.* **49**, 341–347 (2013).
78. You, Y., Richer, E. J., Huang, T. & Brody, S. L. Growth and differentiation of mouse tracheal epithelial cells: selection of a proliferative population. *Am. J. Physiol. Lung Cell Mol. Physiol.* **283**, L1315–L1321 (2002).
79. Langmead, B. & Salzberg, S. L. Fast gapped-read alignment with Bowtie 2. *Nat. Methods* **9**, 357–359 (2012).
80. Quinlan, A. R. & Hall, I. M. BEDTools: a flexible suite of utilities for comparing genomic features. *Bioinformatics* **26**, 841–842 (2010).
81. Wang, Q. et al. Exploring epigenomic datasets by ChIPseeker. *Curr. Protoc.* **2**, e585 (2022).

Acknowledgements

We thank members of the G.K.A., J.E.P., and D.W.L. labs for assistance and support. We also acknowledge the support from NIH (R01AI140758 and R01AI159678 to D.W.L. and P01AI120943 to G.K.A. and D.W.L.). We acknowledge the Genome Technology Access Center at the Washington University McDonnell Genome Institute, which is supported by NCI P30 CA91842 from the NIH National Center for Research Resources and the NIH Roadmap for Medical Research. Beamlines 4.2.2, 8.2.1 and 8.2.2 of the Advanced Light Source, a DOE Office of Science User Facility under Contract No. DE-AC02-05CH11231, are supported in part by the ALS-ENABLE program funded by the NIH National Institute of General Medical Sciences P30 GM124169-01.

Author contributions

D.W.L. conceived of the overall project. D.W.L., J.E.P., and G.K.A. designed the study and managed the experiments and analysis with input from the coauthors. P.K., O.K., G.U., Y.K., Y.H., N.D.W., J.X., J.P., J.C.N., M.L.G., S.L.B., D.B., G.K.A., J.E.P., and D.W.L. performed research and analyzed results. P.K., G.K.A., J.E.P., and D.W.L. wrote the manuscript with input from all coauthors.

Competing interests

The authors declare no competing interests.

Additional information

Supplementary information The online version contains supplementary material available at https://doi.org/10.1038/s41467-025-58216-4.

Correspondence and requests for materials should be addressed to Daisy W. Leung.

Peer review information *Nature Communications* thanks the anonymous, reviewer(s) for their contribution to the peer review of this work. A peer review file is available.

Reprints and permissions information is available at http://www.nature.com/reprints

Publisher's note Springer Nature remains neutral with regard to jurisdictional claims in published maps and institutional affiliations.

Open Access This article is licensed under a Creative Commons Attribution-NonCommercial-NoDerivatives 4.0 International License, which permits any non-commercial use, sharing, distribution and reproduction in any medium or format, as long as you give appropriate credit to the original author(s) and the source, provide a link to the Creative Commons licence, and indicate if you modified the licensed material. You do not have permission under this licence to share adapted material derived from this article or parts of it. The images or other third party material in this article are included in the article's Creative Commons licence, unless indicated otherwise in a credit line to the material. If material is not included in the article's Creative Commons licence and your intended use is not permitted by statutory regulation or exceeds the permitted use, you will need to obtain permission directly from the copyright holder. To view a copy of this licence, visit http://creativecommons.org/licenses/by-nc-nd/4.0/.

© The Author(s) 2025